

**Dissociative Chemisorption of Methane on Ni(111) Using a Chemically Accurate
Fifteen Dimensional Potential Energy Surface**

Xueyao Zhou¹, Francesco Nattino², Yaolong Zhang¹, Jun Chen³, Geert-Jan Kroes^{2,*},
Hua Guo^{4,*}, and Bin Jiang^{1,*}

¹*Department of Chemical Physics, University of Science and Technology of China,
Hefei, Anhui 230026, China*

²*Leiden Institute of Chemistry, Leiden University, Gorlaeus Laboratories, P.O. Box
9502, 2300 RA Leiden, The Netherlands*

³*Collaborative Innovation Center of Chemistry for Energy Materials (iChEM),
College of Chemistry and Chemical Engineering, Xiamen University, Xiamen, Fujian
361005, China*

⁴*Department of Chemistry and Chemical Biology, University of New Mexico,
Albuquerque, New Mexico 87131, USA*

*: corresponding authors: g.j.kroes@chem.leidenuniv.nl, hguo@unm.edu, bjiangch@ustc.edu.cn.

Abstract

A fifteen-dimensional global potential energy surface for the dissociative chemisorption of methane on the rigid Ni(111) surface is developed by a high fidelity fit of $\sim 200,000$ DFT energy points computed using a specific reaction parameter density functional designed to reproduce experimental data. The permutation symmetry and surface periodicity are rigorously enforced using the permutation invariant polynomial-neural network approach. The fitting accuracy of the potential energy surface is thoroughly investigated by examining both static and dynamical attributes of the CHD_3 dissociation on the frozen surface. This potential energy surface is expected to be chemically accurate as after correction for surface temperature effects it reproduces the measured initial sticking probabilities of CHD_3 on Ni(111) for various incidence conditions.

I. Introduction

Surface chemical reactions play a key role in many important areas of research such as heterogeneous catalysis, corrosion and material processing.¹ A quantitative understanding of surface reaction dynamics requires first principles modeling with high accuracy. Currently, however, the reliability of theoretical simulations is limited by the accuracy of density functional theory (DFT) at the generalized gradient approximation (GGA) and meta-GGA levels.² While providing valuable information, standard GGA and meta-GGA density functionals do not offer the high accuracy of either high-level wave function-based *ab initio* methods or hybrid functionals with exact exchange, which have been employed to model gas-phase reactions.^{3, 4} Unfortunately, these methods are not yet applicable to dynamical calculations of gas-surface systems due to their unfavorable scaling with respect to the number of electrons.

Even for single point calculations on molecule-metal surface interactions, stochastic approaches like the quantum-Monte Carlo (QMC)⁵ and correlated wave function approaches with density embedding,⁶⁻⁸ while in principle accurate, still face convergency issues. Recent QMC calculations were able to reproduce the semi-empirical reference value of the $\text{H}_2 + \text{Cu}(111)$ barrier height to within no better than 1.6 kcal/mol, as a result of limitations imposed by fixed node, locality, and time step errors.⁹ The accuracy of correlated wave function approaches with embedding is in practice limited by the size of the embedded cluster that can be modeled.⁶ As a result, it is still challenging to predict surface reaction barrier heights and related

potential energy surfaces (PESs) with chemical accuracy (<1 kcal/mol, or 4.2 kJ/mol, or 43 meV), which has been routinely realized in triatomic and tetratomic systems in the gas phase.¹⁰⁻¹³

Recently, a semi-empirical approach to the accuracy problem was proposed, *i.e.*, specific reaction parameter (SRP) density functional theory.¹⁴ Practically, at first this involved mixing two exchange-correlations functionals, the PW91 functional¹⁵ and the revised-Perdew-Burke-Ernzerhof (RPBE)¹⁶ functional, on the premise that the former tends to overbind while the latter typically underestimates the molecule-surface interaction. For two benchmark systems, namely $\text{H}_2 + \text{Cu}(111)$ ¹⁴ and $\text{H}_2 + \text{Cu}(100)$,¹⁷ both quantum dynamical (QD) and quasi-classical trajectory (QCT) calculations on the fitted SRP PES reproduced experimental dissociative sticking coefficients with chemical accuracy. This SRP density functional was also found to describe reasonably well the rotational quadrupole alignment parameter of D_2 reacting on $\text{Cu}(111)$,¹⁸ and the non-reactive scattering of H_2 from $\text{Cu}(111)$.^{19, 20} This semi-empirical approach is much more efficient than hybrid functionals or higher-level methods since the implementation is still within the GGA-DFT framework.

Extending this approach to describing the interaction between a polyatomic molecule and a metal surface is not a trivial task, due to the increasing number of degrees of freedom (DOFs). Probably the best candidate system for this purpose is methane dissociation on metal surfaces, given the abundant experimental data available.²¹ Also, thanks to the industrial importance of the methane steam reforming

process,²² the dissociative chemisorption of methane on metal surfaces has become one of the most studied gas-surface reactions. Indeed, pioneering quantum state resolved experiments have discovered strong vibrational mode specificity²³⁻²⁹ and bond selectivity,³⁰⁻³² as well as steric effects^{33,34} in methane dissociation, challenging the ability of theoretical models to accurately characterize the dynamics in high dimensionality.

There has been rapid progress in the past several years in developing first-principles based multi-dimensional interaction PESs and in understanding the non-statistical reaction dynamics.^{35,36} For example, Jackson and coworkers advanced a reaction path Hamiltonian (RPH) approach, in which the vibrational DOFs perpendicular to the reaction coordinate are approximated as harmonic but all explicitly involved in the dynamical calculations. This approach has shed valuable light on the mode specificity and bond selectivity of methane dissociation on Ni and Pt.^{37, 38} In 2013, Jiang et al. developed the first DFT-based fully coupled twelve-dimensional (12D) global PES for CH₄+Ni(111) and performed eight-dimensional (8D) QD calculations which semi-quantitatively reproduced experimental sticking coefficients for various initial states of methane.³⁹ This PES was later used to investigate mode specificity and bond selectivity,⁴⁰ as well as steric effects.⁴¹ More recently, Shen et al. have fit thirteen and fifteen-dimensional PESs using neural networks (NNs) for methane dissociative chemisorption on Ni(111) and Ni(100),⁴²⁻⁴⁴ and reported seven-dimensional (7D) to nine-dimensional (9D) QD results which highlighted the importance of the azimuthal angle⁴⁴ and the presence of

multiple dissociation barriers over different impact sites.⁴⁵ These high-dimensional models often neglect surface motion effects, which have however been proven to play an important role in methane dissociation.⁴⁶ These effects can be introduced *a posteriori* through a sudden model as proposed by Jackson and coworkers.^{36, 47, 48} Reactive force fields accounting for surface DOFs have also been reported and they have been used to investigate the bond selectivity of the dissociative chemisorption of methane isotopologues.^{49, 50} Importantly, the mode specific and bond selective behaviors can also be qualitatively rationalized by a simple transition-state based model.⁵¹ Lastly, through a local-density friction approximation model, the effects of electron-hole pair excitations have been examined. These effects were found to give rise to a small reduction in dissociative probabilities for all vibrational states, but they hardly led to changes in the vibrational efficacies.⁵² Nevertheless, none of the aforementioned studies have provided quantitative agreement with experimental data.

Ab initio molecular dynamics (AIMD) calculations were performed in an extensive search for accurate SRP functionals for methane dissociation on Pt(111)^{53, 54} and Ni(111),^{55, 56}. The use of AIMD bypasses the need of constructing high-dimensional PESs, while sacrificing the possibility of a quantum description of the nuclear dynamics, for which a PES is required on practical grounds. Since the surface motion is explicitly taken into account, the AIMD sticking coefficients can be directly compared to experimental data at high collision energies without further corrections. Thus, these calculations can be straightforwardly employed to fit an SRP density functional provided experimental data is available for total energies (incident

+ vibrational) exceeding the classical reaction barrier height. Very recently, it has been shown that AIMD results using the SRP32-vdW functional, with 32% of RPBE exchange and 68% of PBE plus the vdW-DF non-local correlation, reproduced dissociative sticking coefficients for CHD₃ on Ni(111) on a wide range of incidence energies with chemical accuracy.⁵⁶ Furthermore, this functional has been shown to quantitatively describe the dissociation of CHD₃ on both flat and stepped Pt surfaces.⁵⁷

However, a disadvantage of AIMD calculations is that they are computationally expensive. Therefore, accurate AIMD calculations on events that occur with low probability, or require long propagation times or large DFT-setups, are hampered by the slow convergence of the statistical error in classical calculations of probabilities. As a result, it is highly desirable to map out an analytical PES using the SRP32-vdW functional. An analytical PES, in fact, would enable further investigations of the reaction dynamics for this molecule-surface system at an enormously reduced computational cost. Once the PES is obtained, QCT calculations can be run orders-of-magnitude faster than the DFT-based AIMD simulations at many energies. More importantly, the PES will allow us to perform QD calculations and to simulate very recent molecular scattering experiments. Herein, we present such a chemically accurate PES for methane interacting with a rigid Ni(111) surface, including fifteen molecular DOFs describing the vibration, the rotation, as well as the translation of the molecule relative to the rigid surface. The constructed PES accounts for all molecular DOFs and has been validated through QCT calculations, and is amenable to QD

calculations in the future.

II. Computational details

A. Electronic structure calculations

Spin-polarized plane-wave DFT calculations were performed using the Vienna Ab initio Simulation Package (VASP).^{58, 59} We modeled the Ni(111) surface with a 3×3 super cell (1/9 ML coverage) and four-layer slab with the atoms kept at their equilibrium positions. The vacuum space between periodic slabs in the z direction is set to 13 Å. The wavefunction is expanded in terms of plane waves up to a kinetic energy cutoff of 350 eV and core electrons were represented by the projector-augmented wave (PAW) method.^{60, 61} The first Brillouin zone was sampled using a Γ -centered $4 \times 4 \times 1$ k -point grid, which includes 10 non-symmetry-equivalent k -points. A Fermi smearing with a width parameter of 0.1 eV was applied to speed up the convergence. This setup has been previously validated to converge the minimum barrier height to within 0.01 eV with respect to plane-wave cutoff energy, the number of k -points, the surface unit cell size and the number of metal layers.⁵⁶

All energies were computed with an exchange-correlation functional with the following form:⁵⁶

$$E_{XC}^{SRP} = xE_X^{RPBE} + (1-x)E_X^{PBE} + E_C^{vdW-DF}, \quad (1)$$

In other words, the SRP32-vdW functional is obtained by mixing the exchange parts of two commonly used functionals, *i.e.*, PBE⁶² and RPBE,¹⁶ plus the non-local correlation of the vdW-DF,⁶³ which improves the description of the long-range van

der Waals (vdW) forces. x in Eq. (1) is an adjustable parameter and takes the value of 0.32, as fit to the experimental “laser-off” sticking coefficients of CHD_3 on Ni(111) in previous work.⁵⁶ Four minimum energy paths (MEPs) were determined by means of the climbing-image nudged elastic band (CI-NEB) method⁶⁴ using four images from the initial state (CH_4 is placed 4 Å above the surface) towards co-adsorbed CH_3 and H in different orientations, which are considered as the final state. The corresponding transition states were identified as the highest energy images along the MEPs and they were all found to have a single imaginary frequency. Note that all the energy barriers reported here have been corrected by 40 meV in order to account for the finite interaction that the molecule still has with the surface in the asymptotic configuration. *i.e.* at $Z=6.5$ Å,⁵⁶ which has been taken into account in the PES construction.

B. Potential energy surface

A potential energy surface represents the potential energy as a function of the nuclear configuration, and should incorporate the effects of all possible symmetries. Our recently proposed permutation invariant polynomial-neural network (PIP-NN) approach provides a rigorous and efficient representation of the PES and it guarantees the system dependent surface periodicity and the permutation symmetry in the molecule. This strategy has been successfully applied to a variety of gaseous and gas-surface systems.^{65,66} The basic architecture of feed-forward NNs consists of one input layer, one or more hidden layers and an output layer, each of which contains one or more neurons that successively connect the input layer towards the outcome(s) in the output layer. Without loss of generality, the value of k th neuron in the i th layer can

be evaluated from prior neurons as:

$$y_k^i = f_i \left(b_k^i + \sum_{j=1}^{N_{i-1}} \omega_{jk}^i y_j^{i-1} \right), \quad (2)$$

where b_k^i are biases of the k th neurons in the i th layer, ω_{jk}^i are weights that connect the j th neurons in the $(i - 1)$ layer and the k th neurons in the i th layer, which are both parameters to be determined, N_{i-1} is the number of neurons in the $(i - 1)$ th layer, f_i are transfer functions which map the information from the $(i - 1)$ th layer into the i th layer and usually take a non-linear form, providing the flexibility of NNs to fit arbitrary real functions. Note that the energy is given by the single neuron in the output layer, which is connected to the last hidden layer by a linear transfer function.

The input layer of a NN PES often consists of internuclear distances, as in recent work on some gas phase^{67, 68} and gas surface reactions.^{42, 43} However, this conventional NN approach does not naturally satisfy the surface periodicity and the molecular permutation symmetry, which could lead to discontinuity issues in classical trajectory calculations. In our PIP-NN scheme,^{65, 66} both types of symmetry are rigorously enforced. To this end, we first initiate twenty-five primitive functions as follows ($j > i = 1, 2, 3, 4, 5$),

$$G_{1-10} = \exp(-\lambda r_{ij}), \quad (3)$$

$$G_{8+3i} = \left[\cos\left(\frac{4\pi y_i}{a\sqrt{3}}\right) + 2 \cos\left(\frac{2\pi x_i}{a}\right) \cos\left(\frac{2\pi y_i}{a\sqrt{3}}\right) \right] \times G_{10+3i}, \quad (4)$$

$$G_{9+3i} = \left[\sin\left(\frac{4\pi y_i}{a\sqrt{3}}\right) - 2 \cos\left(\frac{2\pi x_i}{a}\right) \sin\left(\frac{2\pi y_i}{a\sqrt{3}}\right) \right] \times G_{10+3i}, \quad (5)$$

$$G_{10+3i} = \exp(-\lambda z_i). \quad (6)$$

Here, G_1 to G_{10} in Eq. (3) consist of exponential functions of ten internuclear

distances in methane, G_{11} to G_{25} in Eqs. (4-6) contain Fourier expansions in terms of atomic lateral coordinates (x_i, y_i) corresponding to the Ni(111) periodicity⁶⁹⁻⁷¹ and exponential functions of z_i , where $i = 1, 2, 3, 4, 5$ correspond to the four H atoms and the C atom in methane. a is the distance between the two nearest Ni atoms in the surface (2.514 Å for Ni(111)). The exponential coefficient $\lambda=1.0 \text{ \AA}^{-1}$ enforces the correct asymptotic behavior of the PES for the CH₄ molecule being far away from the surface, removing in this way the ‘artificial’ periodicity in the Z direction that characterizes the supercell approach in the DFT calculations and making our dynamical calculations below valid.

The next step is to adapt the permutation symmetry due to the four identical H atoms, which is essential for a faithful representation of the PES but not intuitively straightforward. Bowman and coworkers advanced a systematic way to generate PIPs of internuclear distances up to a certain degree for a given molecule in the gas phase, based on the theory of polynomial invariants.^{72, 73} These PIPs form the input layer of PIP-NN in gas phase applications.^{66, 74, 75} For describing molecule-surface interaction, PIPs were generated from the above mentioned primitive functions, where the atomic centered G functions are considered as independent variables. For example, when exchanging H₂ and H₃ atoms, the values of $\{G_{14} - G_{16}\}$ and $\{G_{17} - G_{19}\}$ need to be exchanged, respectively. We have explicitly derived 10 PIPs for H₂/Ag(111)⁷⁶ and 18 PIPs for H₂O/Ni(111)⁷⁷ and CO₂/Ni(100)⁷⁸ in our earlier publications. Here, the situation is more complicated and a total of 320 PIPs up to the sixth degree were derived with the computational algebra software SINGULAR.⁷⁹ These PIPs represent

the minimal generating invariants⁸⁰ of this system based on the 25 primitive functions to yield symmetry invariant polynomials up to an arbitrary degree. Our approach is similar in spirit to that of Shao et al. who used “fundamental invariants” in their work to fit PESs in gas phase.⁸¹ Finally, three additional G functions defined by the center of mass coordinates (X, Y, Z) in the same way as that in Eqs. (4-6) were required to avoid the existence of accidental symmetries between chemically different geometries,⁷¹ resulting in 323 terms (*i.e.*, 3 + 320 PIPs) in the input layer of the PIP-NN.

We started by fitting a primitive PES with the geometries and energies extracted from 1000 AIMD trajectories on the frozen Ni(111) surface computed by Nattino et al.⁵⁶ Since the reaction probability is low, the AIMD trajectories oversample the configuration space in the entrance channel, and barely cover the interaction region and the product channel. To reduce the oversampling in the entrance channel, a geometric criterion based on the root mean square error (RMSE) of the Euclidean distance between two points was applied to exclude points that were too close to each other.⁶⁶ Additional points were sampled by running QCT calculations with various initial conditions on this primitive PES, with a focus on the interaction region and the product channels. Following our earlier work, a newly sampled point is added to the data set only if it satisfies the aforementioned geometric criterion and an additional energetic criterion given by RMSE of the energies predicted by three different fits for this point.⁶⁶ The new data selected in this way were then used to update the PES. This procedure was iterated and the criteria were gradually adjusted. The PES was finally

considered to be converged when the calculated dissociation probability curve no longer changed with respect to the number of points in the data set.

Following such a protocol, a total of 188188 DFT energy points was finally collected. To make sure that the PES gives the correct description of the asymptotic region, we additionally computed ~ 5000 isolated CH_4 configurations whose energies plus the energy of a bare surface were considered as the reference asymptotic energies and added to the data set.

The PIP-NN fitting was performed with these data randomly divided into two sets (training (90%) and validation (10%)) using the Levenberg-Marquardt algorithm⁸² with early stopping. The weight for the i th point in the configuration space was given by $w_i = (E_0 / (E_i + E_0))^3$ with E_0 being the lowest energy in the data set. In order to accurately describe the stationary points, the weights of the configurations that are close to the transition states were kept as unity. The finally converged PES was an average over the three best fits, each of which consists of two hidden layers with 12 and 40 neurons, respectively, denoted as 323-12-40-1 with 4449 parameters in total.

C. Dynamical calculations

QCT calculations were performed with a heavily modified version of the VENUS code.⁸³ Specifically, the gaseous molecule was initially set at 10.0 Å above the metal surface where the molecule-surface interaction is negligible with normal incidence towards the surface and randomly distributed lateral coordinates in the unit cell. To simulate the experiment in Ref. 56, initial vibrational states of CHD_3 under

the laser-off conditions were sampled from a Boltzmann distribution with the vibrational temperature taken equal to the nozzle temperature T_N . In the description of the rotational states, the rotational cooling was taken into account using $T_{rot} \approx 0.0247T_N$, as given in experiments. Note that the angular momentum was initially set to zero in the laser-off calculations in Ref. 47, but this is not expected to affect the comparison between the two datasets since the rotational temperature is always low. For molecules with the C-H stretching mode excited with one quantum, *i.e.*, $\text{CHD}_3(\nu_1=1)$, and for the vibrationally excited molecules in the simulated laser-off experiment, a standard normal mode sampling method was adopted. For $\text{CHD}_3(\nu_1=1)$, the rotational state was described as a symmetric top with $J=2$, $K=0$. The molecular orientation was randomly chosen, as the experiments should sample collisions of methane in a statistical distribution of M -states (± 2 , ± 1 , and 0) with the surface.⁵⁶ The trajectories were propagated using a time step of 0.1 fs. A trajectory was terminated if either a C-H or C-D bond stretched to 2.2 Å, and then counted as reactive event; otherwise, was considered as scattered if the molecule reached 10.1 Å with the velocity pointing away from the metal surface. To achieve reasonably small statistical errors (relative error of a few percent), up to 3×10^6 trajectories were computed at the lowest collision energy.

The surface temperature dependent dissociative sticking coefficients were obtained from the static surface dissociation probabilities using Jackson's lattice relaxed sudden (LRS) model.^{36, 48} Following the work of Tiwari et al.,⁴⁸ the changes of barrier location and height with the vertical motion of the surface atom closest to

the molecule at the transition state can be described in terms of two types of couplings. One is the “electronic coupling”, in which the barrier height changes linearly with the perpendicular displacement of the Ni atom nearest to, and below the methane molecule (Q), *i.e.*, $\Delta E_a = -\beta Q$. Here, Q is taken relative to the top surface layer, with all other metal atoms frozen in their ideal lattice positions. This effect was taken into account by averaging the reaction probabilities calculated at various displacements Q under the assumption that the Q -dependent reaction probability curves can be obtained from the static surface one through an energy shift equal to $-\beta Q$. The other effect is the “mechanical coupling”, which accounts for the shift of the transition state along the Z axis with Q : $\Delta Z_{TS} = \alpha Q$, where $\alpha = \Delta Z_{TS} / Q_{TS}$ corresponds to the ratio between the Z shift of the transition state and the surface atom displacement Q . This effect was treated using a modified surface mass model with $M'_s = M_s / \alpha^2$ (M_s is the mass of a Ni atom), which means that the lattice atom momentum (P) conjugate to Q is accounted for by replacing the molecule’s collision velocity with the relative collision velocity. In the original surface mass model, $\alpha=1.0$.⁸⁴ The phonon parameters estimated using the SRP32-vdW functional have been found to be quite similar to the model values from Ref. 48, which were $\alpha=0.69$ and $\beta=1.16$ eV/Å. We have therefore used these values in this work.

III. Results and Discussion

A. Potential energy surface

Before discussing the features of the 15D PES, we first present the accuracy of our fit with respect to the number of neurons in each hidden layer. In Fig. 1, we

compare the computed dissociation probabilities for CHD_3 on Ni(111) under “laser-off” conditions⁵⁶ with three different NN fits, *i.e.*, 323-5-40-1, 323-12-40-1, and 323-20-40-1, which are labeled as PES1, PES2, and PES3, respectively. Considering that our aim here is to test the convergence of the NN-PES with respect to the number of points employed in the fit, we have performed laser-off beam simulations making use of one and the same value nozzle temperature ($T_N=550$ K) for the entire range of incidence energies. It is clear that the results obtained with PES2 and PES3 agree quite well with each other, while PES1 slightly underestimates the reactivity. This validates the accuracy of PES2 which contains fewer parameters and is thus more efficient to use than PES3. On the other hand, with the same 323-12-40-1 structure, two additional NN fits (PES4, PES5) were made training with roughly 1×10^4 and 2×10^4 fewer DFT points randomly excluded from the full set. It can be seen from Fig. 1 that dynamics on PES4 reproduces the results obtained with the full set (PES2) well, but with PES5 the dissociation probability is significantly underestimated at low energies. These two tests suggest that our final NN fit (PES2) is well converged with respect to both the number of neurons and data points.

We next analyze the potential energy and fitting error distribution in the NN fit, as shown in Fig. 2. It is evident that most selected points have energies that fall broadly into the range [0.0-3.5] eV, which is most relevant to the dissociation dynamics. More importantly, the PIP-NN PES reproduced $\sim 98\%$ of the points with rather small deviations (less than 50 meV) and more than half of the points have an error ≤ 10 meV. This leads to an overall RMSE of only 15.3 meV. In particular, the

RMSE in the entrance channel ($Z_C > 2.5 \text{ \AA}$) where the energy corrugation is small, is only 8.8 meV, as compared to a RMSE of 20.2 meV in the interaction and product regions ($Z_C \leq 2.5 \text{ \AA}$) where the potential energy varies more drastically. These results demonstrate the high global fitting accuracy of the PIP-NN PES.

In addition to the global fitting accuracy, the local topography of the PES needs to be reproduced well. In previous work, four distinct first-order transition states (TSs) were identified with the SRP32-vdW functional, which are roughly located over the top site.⁵⁶ These four TSs are rather similar to each other, having one C-H bond extended to $\sim 1.6 \text{ \AA}$ (a “late” barrier) while differing in the relative orientation of the CH_3 moiety with respect to the dissociating C-H bond and in the azimuthal orientation of the molecule with respect to the surface normal. As displayed in Fig. 3, specifically, the dissociating C-H bond can point towards either a fcc or a hcp site, with either one C-H bond or two C-H bonds pointing away from the surface. One expects the four barrier heights corresponding to these TSs to be quite close to each other as the PES is relatively flat with respect to the two rotational angles described. Reproducing these energies and geometries is therefore a good test for the quality of the fit.

Table I compares the most important TS coordinates and barrier heights obtained from the PES and the DFT optimizations. The activation energies reported here are computed as $E_b = \epsilon_{TS} - \epsilon_{asym}$, where ϵ_{TS} and ϵ_{asym} are the absolute energy at the TS and the asymptotic configuration, respectively. All four TS structures are well reproduced with discrepancies in Z_C and r_{CH} smaller than 0.016 \AA and in θ smaller than 0.8° . The barrier heights are also well reproduced with small deviations within

~ 2.7 meV. Even the order of the barrier heights, which vary over an energy range spanning less than 20 meV, is reproduced. Moreover, the two-dimensional (2D) minimum energy cuts calculated either directly from DFT constrained optimizations or from the NN PES are compared as a function of Z_C and r_{CH} with the other coordinates optimized. As shown in Fig. 4, the two plots are almost identical, which demonstrates that our fit reproduces the DFT data perfectly in both the topography and absolute energy.

In addition to reproducing well the DFT saddle points, this PES has a new feature different from previous ones, *i.e.*, a physisorption well due to the inclusion of vdW effects in the density functional employed. Our fitted well depth (187 meV) reproduces the well depth from DFT calculations (196 meV) rather well,⁵⁶ and is in reasonable agreement with the experimental estimate of 124 meV.^{85, 86} All the analysis performed indicates that the present PES describes the raw SRP32-vdW DFT data with high fidelity, thereby preserving the high accuracy inherent in the use of the SRP32-vdW functional.

Now let us compare the specific reaction pathways at selected high symmetry sites. It has been found that in water dissociation on Ni(111), while the top site features a much lower barrier than the bridge and hollow sites, it is the least reactive site at high incident energies because it is too tight and ineffective for energy transfer from translational energy to the reaction coordinate.⁷⁷ This feature is largely determined by the topography of the site-specific PES near the transition state,^{87, 88} suggesting the importance of the multi-dimensionality of the PES. In the case of

methane dissociation here, the barrier heights are found to be 1.04 eV (top), 1.36 eV (bridge), and 1.33 eV (fcc), respectively. In addition, 2D contour plots as a function of the height of the CH₄ center of mass (Z_{com}) and r_{CH} at top, bridge, and fcc sites are compared in Fig. 5. Interestingly, the transition states at these sites are all relatively loose in the sense that the potential energy increases moderately with respect to the direction perpendicular to the reaction coordinate. The ‘accessibility’ of the transition states is therefore not expected to limit the reactivity of any of the sites, in contrast with what has been observed for water dissociation. Recent high-dimensional QD calculations using a 15D PES have indicated that the bridge and fcc sites are always less reactive than the top site with the reaction probability being shifted towards higher energies by the difference in barrier height,^{44, 45} which is consistent with the picture we present here.

B. Initial sticking probabilities of CHD₃

With the analytical PES, it is computationally inexpensive to compute reaction probabilities for CHD₃ dissociation on Ni(111) down to $\sim 10^{-6}$ at the lowest incident energy, which is presently not feasible with AIMD calculations. The dissociation probability of CHD₃ has first been computed on the frozen surface, after which lattice effects have been incorporated using Jackson’s LRS model.^{36, 48} To enable a straightforward comparison with the AIMD and experimental data at specific energies, the translational velocity spread in the molecular beam has been taken into account by averaging the energy-dependent dissociation probability over the experimental velocity distribution,⁸⁹

$$P_0(E_{avg}) = \int_{v=0}^{v=\infty} f(v)P_0(E_i)dv / \int_{v=0}^{v=\infty} f(v)dv, \quad (7)$$

where $P_0(E_i)$ is the reaction probability computed for a specific incidence energy $E_i=mv^2/2$, $f(v)$ is the velocity distribution given by $f(v) = v^3 \exp(-[(v-v_0)/\alpha]^2)$, in which v is the incident velocity, v_0 is the stream velocity and α is the width parameter. The values of v_0 and α were taken from Ref. 56, as obtained by fitting an appropriate expression to time-of-flight (TOF) spectra recorded for the various molecular beams used. Fig. 6 shows the frozen surface reaction probability (P_0) of CHD_3 as a function of the incidence energy. It should be noted that we have simulated the same nozzle temperature of 600 K over the entire energy range in order to highlight the effect of velocity averaging. This produces good agreement with the corresponding AIMD result at 112 kJ/mol.⁵⁶ It is interesting to note that the velocity averaging seems to increase the reactivity slightly, which implies that the high-energy contributions to the velocity-averaged reaction probability are more significant.

To consider the influence of lattice motion, we should, ideally, average the static surface dissociation probability over the surface atom displacements of a mobile surface. In the more approximate LRS model we use here, instead we average the reaction probability over the vibrational motion perpendicular to the surface of only one, *i.e.*, the nearest surface atom (with the coordinate Q) to account for the “electronic coupling”, and over its conjugated momentum (P) to account for the “mechanical coupling”. Guo and Jackson⁹⁰ recently discussed two models to describe the vertical displacements of the surface atoms within the LRS framework. One way

consists in sampling Q from a Boltzmann distribution at a given surface temperature (T_s) using the frequency calculated for the vertical displacement of a single surface atom relative to a fixed surface (“Einstein model”). This model has been argued to underestimate the root mean square vibrational amplitude orthogonal to the surface of the first layer atoms ($Q_{rms,\perp}$) in a mobile surface.⁹⁰ Alternatively, one can sample Q from a Gaussian distribution with width $Q_{rms,\perp}$ as readily calculated from the experimentally measured surface Debye temperature ($\theta_{D\perp}$),⁹¹

$$Q_{rms,\perp}^2(T_s) = \frac{3N_A \hbar^2 T_s}{M_s k_B \theta_{D\perp}^2}, \quad (8)$$

where N_A is Avogadro’s constant, \hbar and k_B are the reduced Planck and Boltzmann constants, respectively, T_s is the surface temperature, M_s is the atomic weight and $\theta_{D\perp} = 220\text{K}$ is the surface Debye temperature in the direction normal to the Ni(111) surface (taken from Ref. 92). This is referred to the “Debye model”, and should yield the correct mean square displacement of the vibrating atom in a mobile (“thermal”) surface.

In Fig.7 we compare the two initial sticking probabilities (S_0) obtained with the same mechanical coupling treatment but varying the model employed to sample Q for the electronic coupling contribution. We simulate a surface temperature $T_S=550\text{ K}$ while modelling again laser-off conditions with the same nozzle temperature for all incidence energies ($T_N=550\text{ K}$). As discussed earlier in the literature,⁹⁰ the “electronic coupling” significantly increases the reactivity, especially at low E_i , due to the thermally assisted dissociation: lower barriers are in fact encountered for the configurations with the surface atom moving outside the surface plane. The

“mechanical coupling” instead decreases the reactivity at high E_i due to the recoil effect. Because of the larger displacements sampled in the Debye model and the greater importance of electronic coupling at low energies, more significant enhancement of the sticking probability is observed at low energies, consistent with the findings of Guo and Jackson in the study of CH_4 dissociation on Pt(111).⁹³

Finally, we compare sticking probabilities for both “laser-off” conditions (modelling the experimental nozzle temperatures) and vibrationally excited ($\nu_1=1$, $J=2$) CHD_3 to AIMD and experimental data. As shown in Fig 8, it is clear that our quasi-classical results obtained on the accurate neural network fitted PES with the frozen surface approximation and corrected for surface temperature effects successfully reproduce AIMD and experimental data in this energy range, especially for vibrationally excited CHD_3 . The agreement between the QCT results corrected for surface motion on the one hand, and the AIMD and experimental results on the other hand, is less good for laser-off reaction at low incidence energies. Interestingly, better agreement is obtained by using the Einstein model, which, however, was argued to be less accurate to describe the root mean square displacement of all surface atoms than the Debye model.

One possible reason is that the QCT method within its static surface implementation still suffers artificial zero point energy violation, *i.e.*, spurious vibrational zero-point energy flow to the reaction coordinate leading to the overestimation of the reactivity near the reaction threshold. The reaction probability on the frozen surface would then be somewhat too high at low incidence energies,

also leading to too high sticking coefficients after the Q -averaging with the Debye model, and explaining the discrepancies seen in Fig. 8. To confirm this, accurate QD calculations accessing the low energy region are needed.

Another possibility is that the “Debye implementation” is less appropriate than the “Einstein implementation” of the LRS model to describe surface temperature effects on reaction near the reaction threshold energy. In the Einstein implementation, the values of α and β correspond well with the underlying model of a single surface atom vibrating against a surface otherwise held fixed, even though the vibrational amplitude underestimates the value obtainable for an actual mobile surface. In the Debye implementation, the vibrational amplitude of the surface atom corresponds well with that of the mobile surface. However, the improved description of the lattice motion is not consistent with the approximation underlying the LSR model (*i.e.* that a single surface atom affects the barrier height through its vibration in an otherwise frozen surface). Including the larger vibrational amplitude that arises from the description of a fully mobile surface in a model that accounts only for the single surface atom vibration having the largest effect on the reaction barrier is likely to give rise to a too high reactivity, as we seem to observe here.

In future, we hope to investigate a model in which the vibrational amplitude of the surface atom is that of an actual mobile surface, while α and β are properly averaged over the motion of the other surface atoms. We expect that such a model should be able to yield improved results for laser-off reaction near the reaction threshold. We note, however, that the QCT method using the NN fit of the PES with

the present model for surface motion is capable of a very good description of the reaction of vibrationally excited CHD₃, and of the AIMD results for laser-off reaction at high incidence energies. This is yet another proof of the accuracy of the NN fit of the SRP32-vdW PES, and suggests that this PES should be quite useful for QD calculations exploring the reaction under conditions in the quantum regime.

IV. Concluding remarks

To summarize, we report a new and accurate fifteen-dimensional PES for the CH₄+Ni(111) system with the aim of enabling a quantitative description of the methane dissociative chemisorption on Ni(111), provided that surface motion is taken into account in a suitable manner as described here. The PES has been fitted to nearly 200,000 DFT energy points computed with the newly developed SRP32-vdW functional,⁵⁶ which incorporates vdW effects and has been shown to enable a chemically accurate description of CHD₃ dissociation on Ni(111) for conditions under which the total molecular energy (incident + vibrational) exceeds the classical barrier height. Millions of quasi-classical trajectories have been computed on this analytical PES in a wide energy range, yielding very good agreement with both AIMD and experimental data, after the lattice effects are accounted for through a simple sudden model proposed by Jackson and coworkers.⁹⁰ As a result, this 15D PES is to our knowledge at present the most accurate PES available for this important system, enabling future high-dimensional QD calculations of dissociation, inelastic scattering and diffraction.⁹⁴

Acknowledgements: This work was supported by National Key R&D Program of China (2017YFA0303500 to B.J.), National Natural Science Foundation of China (91645202, 21722306, and 21573203 to B.J.), Fundamental Research Funds for the Central Universities of China (WK2060190082 and WK2340000078 to B.J.), U. S. National Science Foundation (CHE-1462019 to H. G.), and an ERC2013 advanced grant (Nr. 338580) and a NWO-CW TOP grant to G. J. K.. J. C. thanks the support of China Postdoctoral Science Foundation (Grant No. 2016M600500) and National Postdoctoral Program for Innovative Talents. Part of calculations have been done at the Supercomputing Center of USTC and National Supercomputing Center in Guangzhou. B. J. thanks Prof. Bret Jackson and Dr. Han Guo for their kind help on the models to account for lattice effects, and we thank Mr. Davide Migliorini for performing part of the single-point DFT calculations needed to fit the PES.

References

1. X. Yang and A. M. Wodtke, *Chem. Soc. Rev.*, 2016, 45, 3573.
2. G.-J. Kroes, *J. Phys. Chem. Lett.*, 2015, 6, 4106.
3. J. J. Zheng, Y. Zhao and D. G. Truhlar, *J. Chem. Theo. Comput.*, 2009, 5, 808.
4. R. Peverati and D. G. Truhlar, *Phil. Trans. R. Soc. A*, 2014, 372, 20120476.
5. W. A. Lester, L. Mitas and B. Hammond, *Chem. Phys. Lett.*, 2009, 478, 1.
6. F. Libisch, C. Huang, P. L. Liao, M. Pavone and E. A. Carter, *Phys. Rev. Lett.*, 2012, 109, 198303.
7. F. Libisch, J. Cheng and E. A. Carter, *Z. Phys. Chem.*, 2013, 227, 1455.
8. F. Göttl, C. Houriez, M. Guitou, G. Chambaud and P. Sautet, *J. Phys. Chem. C*, 2014, 118, 5374.
9. K. Doblhoff-Dier, J. Meyer, P. E. Hoggan and G. J. Kroes, *J. Chem. Theo. Comput.*, 2017, 13, 3208.
10. M. Qiu, Z. Ren, L. Che, D. X. Dai, S. Harich, X. Wang, X. Yang, C. Xu, D. Xie, M. Gustafsson, R. T. Skodje, Z. Sun and D. H. Zhang, *Science*, 2006, 311, 1440.
11. C. Xiao, X. Xu, S. Liu, T. Wang, W. Dong, T. Yang, Z. Sun, D. Dai, X. Xu, D. H. Zhang and X. Yang, *Science*, 2011, 333, 440.
12. X. Wang, W. Dong, C. Xiao, L. Che, Z. Ren, D. Dai, X. Wang, P. Casavecchia, X. Yang, B. Jiang, D. Xie, Z. Sun, S.-Y. Lee, D. H. Zhang, H.-J. Werner and M. H. Alexander, *Science*, 2008, 322, 573.
13. Y. Li, Z. Sun, B. Jiang, D. Xie, R. Dawes and H. Guo, *J. Chem. Phys.*, 2014, 141, 081102.
14. C. Díaz, E. Pijper, R. A. Olsen, H. F. Busnengo, D. J. Auerbach and G.-J. Kroes, *Science*, 2009, 326, 832.
15. J. P. Perdew, J. A. Chevary, S. H. Vosko, K. A. Jackson, M. R. Pederson, D. J. Singh and C. Fiolhais, *Phys. Rev. B*, 1992, 46, 6671.
16. B. Hammer, L. B. Hansen and J. K. Nørskov, *Phys. Rev. B*, 1999, 59, 7413.
17. L. Sementa, M. Wijzenbroek, B. J. van Kolck, M. F. Somers, A. Al-Halabi, H. F. Busnengo, R. A. Olsen, G. J. Kroes, M. Rutkowski, C. Thewes, N. F. Kleimeier and H. Zacharias, *J. Chem. Phys.*, 2013, 138, 044708.
18. F. Nattino, C. Díaz, B. Jackson and G.-J. Kroes, *Phys. Rev. Lett.*, 2012, 108, 236104.
19. C. Diaz, R. A. Olsen, D. J. Auerbach and G.-J. Kroes, *Phys. Chem. Chem. Phys.*, 2010, 12, 6499.
20. G. J. Kroes, C. Diaz, E. Pijper, R. A. Olsen and D. J. Auerbach, *PNAS*, 2010, 107, 20881.
21. R. D. Beck and A. L. Utz, in *Dynamics of Gas-Surface Interactions*, edited by R. D. Muiño and H. F. Busnengo Springer, Heidelberg, 2013.
22. G. Jones, J. G. Jacobsen, S. S. Shim, J. Kleis, M. P. Andersson, J. Rossmeisl, F. Abild-Pedersen, T. Bligaard, S. Helveg, B. Hinneman, J. R. Rostrup-Nielsen, I. Chorkendorff, J. Sehested and J. K. Nørskov, *J. Catal.*, 2008, 259, 147.
23. L. B. F. Juurlink, D. R. Killelea and A. L. Utz, *Prog. Surf. Sci.*, 2009, 84, 69.
24. R. R. Smith, D. R. Killelea, D. F. DelSesto and A. L. Utz, *Science*, 2004, 304,

992.

25. L. B. F. Jurlink, P. R. MaCabe, R. R. Smith, C. L. DeCologero and A. L. Utz, *Phys. Rev. Lett.*, 1999, 83, 868.
26. R. Bisson, M. Sacchi, T. T. Dang, B. Yoder, P. Maroni and R. D. Beck, *J. Phys. Chem. A*, 2007, 111, 12679.
27. P. Maroni, D. C. Papageorgopoulos, M. Sacchi, T. T. Dang, R. D. Beck and T. R. Rizzo, *Phys. Rev. Lett.*, 2005, 94, 246104.
28. R. D. Beck, P. Maroni, D. C. Papageorgopoulos, T. T. Dang, M. P. Schmid and T. R. Rizzo, *Science*, 2003, 302, 98.
29. M. P. Schmid, P. Maroni, R. D. Beck and T. R. Rizzo, *J. Chem. Phys.*, 2002, 117, 8603.
30. P. M. Hundt, H. Ueta, M. E. van Reijzen, B. Jiang, H. Guo and R. D. Beck, *J. Phys. Chem. A*, 2015, 119, 12442.
31. L. Chen, H. Ueta, R. Bisson and R. D. Beck, *Faraday Disc.*, 2012, 157, 285.
32. D. R. Killelea, V. L. Campbell, N. S. Shuman and A. L. Utz, *Science*, 2008, 319, 790.
33. B. L. Yoder, R. Bisson, P. M. Hundt and R. D. Beck, *J. Chem. Phys.*, 2011, 135, 224703.
34. B. L. Yoder, R. Bisson and R. D. Beck, *Science*, 2010, 329, 553.
35. B. Jiang, M. Yang, D. Xie and H. Guo, *Chem. Soc. Rev.*, 2016, 45, 3621.
36. H. Guo, A. Farjamnia and B. Jackson, *J. Phys. Chem. Lett.*, 2016, 7, 4576.
37. B. Jackson and S. Nave, *J. Chem. Phys.*, 2011, 135, 114701.
38. B. Jackson and S. Nave, *J. Chem. Phys.*, 2013, 138, 174705.
39. B. Jiang, R. Liu, J. Li, D. Xie, M. Yang and H. Guo, *Chem. Sci.*, 2013, 4, 3249.
40. B. Jiang and H. Guo, *J. Phys. Chem. C*, 2013, 117, 16127.
41. B. Jiang and H. Guo, *J. Phys. Chem. C*, 2016, 120, 8220.
42. X. J. Shen, J. Chen, Z. J. Zhang, K. J. Shao and D. H. Zhang, *J. Chem. Phys.*, 2015, 143, 144701.
43. X. Shen, Z. Zhang and D. H. Zhang, *Phys. Chem. Chem. Phys.*, 2015, 17, 25499.
44. X. Shen, Z. Zhang and D. H. Zhang, *J. Chem. Phys.*, 2016, 144, 101101.
45. X. Shen, Z. Zhang and D. H. Zhang, *J. Chem. Phys.*, 2017, 147, 204702.
46. S. Nave and B. Jackson, *Phys. Rev. Lett.*, 2007, 98, 173003.
47. S. Nave, A. K. Tiwari and B. Jackson, *J. Phys. Chem. A*, 2014, 118, 9615.
48. A. K. Tiwari, S. Nave and B. Jackson, *J. Chem. Phys.*, 2010, 132, 134702.
49. A. Lozano, X. J. Shen, R. Moiraghi, W. Dong and H. F. Busnengo, *Surf. Sci.*, 2015, 640, 25.
50. X. J. Shen, A. Lozano, W. Dong, H. F. Busnengo and X. H. Yan, *Phys. Rev. Lett.*, 2014, 112, 046101.
51. H. Guo and B. Jiang, *Acc. Chem. Res.*, 2014, 47, 3679.
52. X. Luo, B. Jiang, J. I. Juaristi, M. Alducin and H. Guo, *J. Chem. Phys.*, 2016, 145, 044704.
53. F. Nattino, D. Migliorini, M. Bonfanti and G.-J. Kroes, *J. Chem. Phys.*, 2016, 144, 044702.
54. F. Nattino, H. Ueta, H. Chadwick, M. E. van Reijzen, R. D. Beck, B. Jackson, M.

- C. van Hemert and G. J. Kroes, *J. Phys. Chem. Lett.*, 2014, 5, 1294.
55. B. Jackson, F. Nattino and G.-J. Kroes, *J. Chem. Phys.*, 2014, 141, 054102
56. F. Nattino, D. Migliorini, G.-J. Kroes, E. Dombrowski, E. A. High, D. R. Killelea and A. L. Utz, *J. Phys. Chem. Lett.*, 2016, 7, 2402.
57. D. Migliorini, H. J. Chadwick, F. Nattino, A. Gutiérrez-González, E. Dombrowski, E. A. High, H. Guo, A. L. Utz, B. E. Jackson, R. D. Beck and G.-J. Kroes, *J. Phys. Chem. Lett.*, 2017, 8, 4177.
58. G. Kresse and J. Furthmuller, *Phys. Rev. B*, 1996, 54, 11169.
59. G. Kresse and J. Furthmuller, *Comp. Mater. Sci.*, 1996, 6, 15.
60. P. E. Blochl, *Phys. Rev. B*, 1994, 50, 17953.
61. G. Kresse and D. Joubert, *Phys. Rev. B*, 1999, 59, 1758.
62. J. P. Perdew, K. Burke and M. Ernzerhof, *Phys. Rev. Lett.*, 1996, 77, 3865.
63. M. Dion, H. Rydberg, E. Schröder, D. C. Langreth and B. I. Lundqvist, *Phys. Rev. Lett.*, 2004, 92, 246401.
64. G. Henkelman, B. P. Uberuaga and H. Jónsson, *J. Chem. Phys.*, 2000, 113, 9901.
65. B. Jiang and H. Guo, *J. Chem. Phys.*, 2014, 141, 034109.
66. B. Jiang, J. Li and H. Guo, *Int. Rev. Phys. Chem.*, 2016, 35, 479.
67. J. Chen, X. Xu and D. H. Zhang, *J. Chem. Phys.*, 2013, 138, 154301.
68. J. Chen, X. Xu, X. Xu and D. H. Zhang, *J. Chem. Phys.*, 2013, 138, 221104.
69. J. Ludwig and D. G. Vlachos, *J. Chem. Phys.*, 2007, 127, 154716.
70. J. Behler, S. Lorenz and K. Reuter, *J. Chem. Phys.*, 2007, 127, 014705.
71. J. Meyer, Ph. D. Thesis, Freie Universität Berlin, 2011.
72. Z. Xie and J. M. Bowman, *J. Chem. Theo. Comp.*, 2010, 6, 26.
73. B. J. Braams and J. M. Bowman, *Int. Rev. Phys. Chem.*, 2009, 28, 577.
74. B. Jiang and H. Guo, *J. Chem. Phys.*, 2013, 139, 054112.
75. J. Li, B. Jiang and H. Guo, *J. Chem. Phys.*, 2013, 139, 204103.
76. B. Jiang and H. Guo, *Phys. Chem. Chem. Phys.*, 2014, 16, 24704.
77. B. Jiang and H. Guo, *Phys. Rev. Lett.*, 2015, 114, 166101.
78. B. Jiang and H. Guo, *J. Chem. Phys.*, 2016, 144, 091101.
79. G.-M. Greuel, G. Pfister and H. Schönemann, (SINGULAR 3-1-6 ---A computer algebra system for polynomial computations, 2012, see <http://www.singular.uni-kl.de>).
80. D. Opalka and W. Domcke, *J. Chem. Phys.*, 2013, 138, 224103.
81. K. Shao, J. Chen, Z. Zhao and D. H. Zhang, *J. Chem. Phys.*, 2016, 145, 071101.
82. M. T. Hagan and M. B. Menhaj, *IEEE Trans. Neural Networks*, 1994, 5, 989.
83. X. Hu, W. L. Hase and T. Pirraglia, *J. Comp. Chem.*, 1991, 12, 1014.
84. M. Hand and J. Harris, *J. Chem. Phys.*, 1990, 92, 7610.
85. J. D. Beckerle, Massachusetts Institute of Technology, 1988.
86. J. D. Beckerle, A. D. Johnson, Q. Y. Yang and S. T. Ceyer, *J. Chem. Phys.*, 1989, 91, 5756.
87. T. Liu, B. Fu and D. H. Zhang, *J. Chem. Phys.*, 2013, 139, 184705.
88. T. Liu, B. Fu and D. H. Zhang, *J. Chem. Phys.*, 2014, 140, 144701.
89. G.-J. Kroes and C. Diaz, *Chem. Soc. Rev.*, 2016, 45, 3658.
90. H. Guo and B. Jackson, *J. Chem. Phys.*, 2016, 144, 184709.

91. H. B. Lyon and G. A. Somorjai, *J. Chem. Phys.*, 1966, 44, 3707.
92. A. Grudniewski and S. Mroz, *J. Phys. C: Solid State Phys.*, 1985, 18, 3387.
93. H. Guo and B. Jackson, *Private communication*.
94. A. Al Taleb and D. Farias, *Phys. Chem. Chem. Phys.*, 2017, 19, 21267.

Table I. Geometries and barrier heights with and without the zero-point energy (ZPE) correction (E_b and E_b^{ZPE} , in meV) for the four transition states shown in Fig. 3 from the NN-PES and DFT calculations in Ref. 56.

	PIP-NN PES					DFT(SRP32-vdW)				
	Z_C (Å)	r_{CH} (Å)	θ (°)	E_b	E_b^{ZPE}	Z_C (Å)	r_{CH} (Å)	θ (°)	E_b	E_b^{ZPE}
C2	2.176	1.611	135.5	1016.73	898.26	2.176	1.606	135.7	1014.66	893.40
B1	2.164	1.634	134.5	1033.78	890.87	2.169	1.638	134.6	1031.24	902.73
B2	2.173	1.614	135.5	1025.52	886.51	2.175	1.612	135.6	1022.95	899.62
C1	2.155	1.625	133.9	1026.66	896.91	2.171	1.632	134.7	1023.99	896.51

Figure captions:

Fig. 1 Reaction probabilities of CHD_3 dissociation as the function of the collision energy in laser-off condition (nozzle temperature 550 K) calculated on different PESs.

Fig. 2 (a) Distribution of DFT points as a function of the potential energy, (b) Distribution of energy errors between the PIP-NN PES and DFT calculations.

Fig. 3. Top view of the four TS configurations, (a) to (d), refer to structures of C2, B1, B2, C1 in Ref. 56 and the side view of C2 (e) to define the structural parameters listed in Table I : Z_C (the distance from the C atom to metal surface), r_{CH} (the length of the dissociating C-H bond) and θ (the polar angle between the dissociating C-H bond and surface normal).

Fig. 4. Comparison of the two-dimensional PES cut as a function of Z_C and r_{CH} between the PIP-NN PES fitted in this work and the SRP32-vdW results from Ref. 56, with other coordinates relaxed.

Fig. 5. Contour plots of the $\text{CH}_4 + \text{Ni}(111)$ PES as a function of the CH_4 mass center (Z_{com}) and r_{CH} on the top (a), bridge (b) and fcc (c) sites, with other coordinates relaxed.

Fig. 6. Comparison of the CHD_3 dissociation reaction probability on the frozen surface PES (PESFS). The black squares correspond to the results obtained on the PIP-NN PES and they are fit to the black dash line, the red dot accounts for the effect of translational velocity spread (PESFS-Velocity averaged), the blue triangle is the FS AIMD result taken from Ref. 56 (AIMDFS).

Fig. 7. Effects of the electronic (Q -averaged) and mechanical couplings (P -averaged), on the CHD_3 dissociation probability with $T_N=550$ K. The Einstein and Debye models (see text for definition) for treating electronic coupling are compared.

Fig. 8. Comparison of calculated CHD_3 initial sticking probabilities obtained from the PIP-NN PES (with the two sudden models), AIMD simulations,⁵⁶ and experiment data⁵⁶ of the laser-off sample and vibrationally excited state ($\nu_1=1, J=2$). The dotted curves corresponding to the experimental fits are shown to guide eyes.

Fig. 1

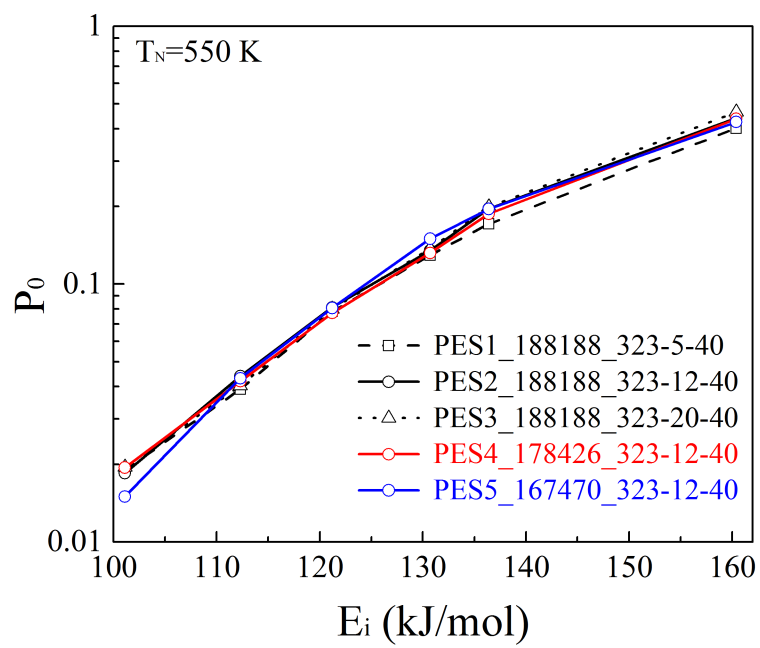


Fig. 2

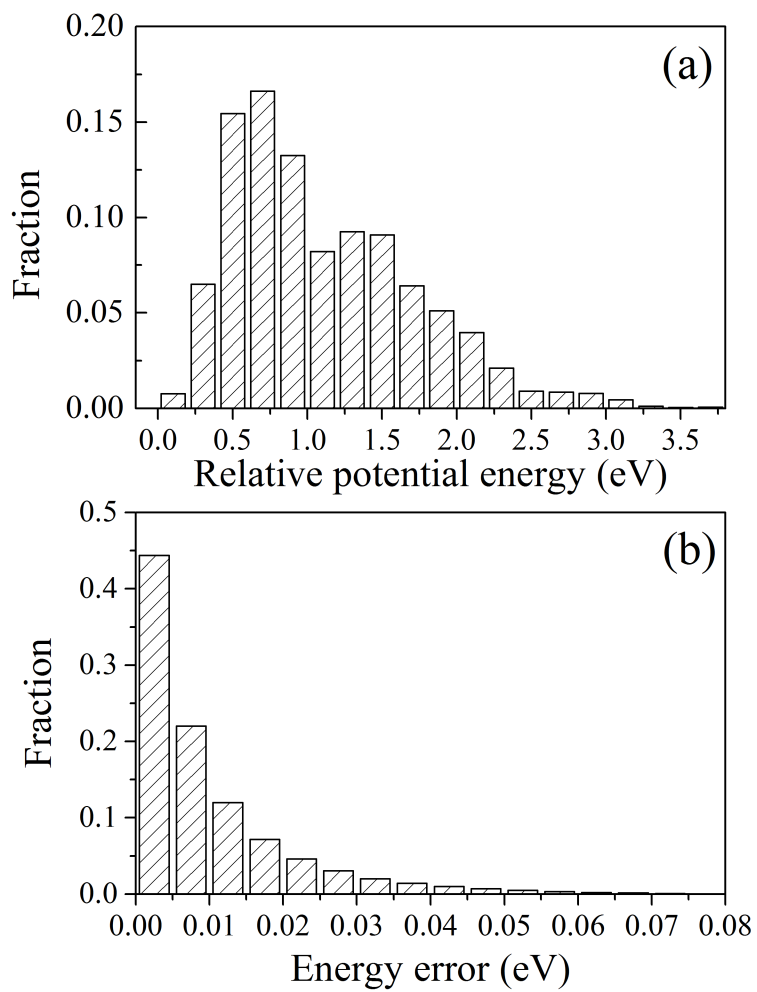


Fig. 3

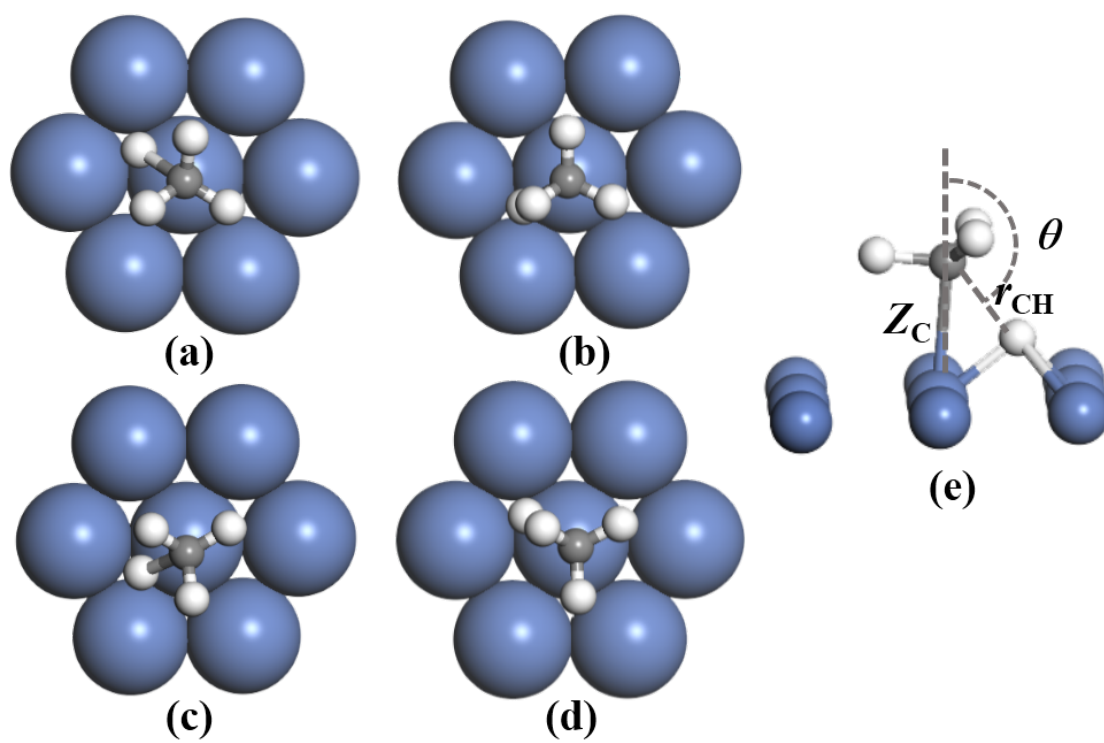


Fig. 4

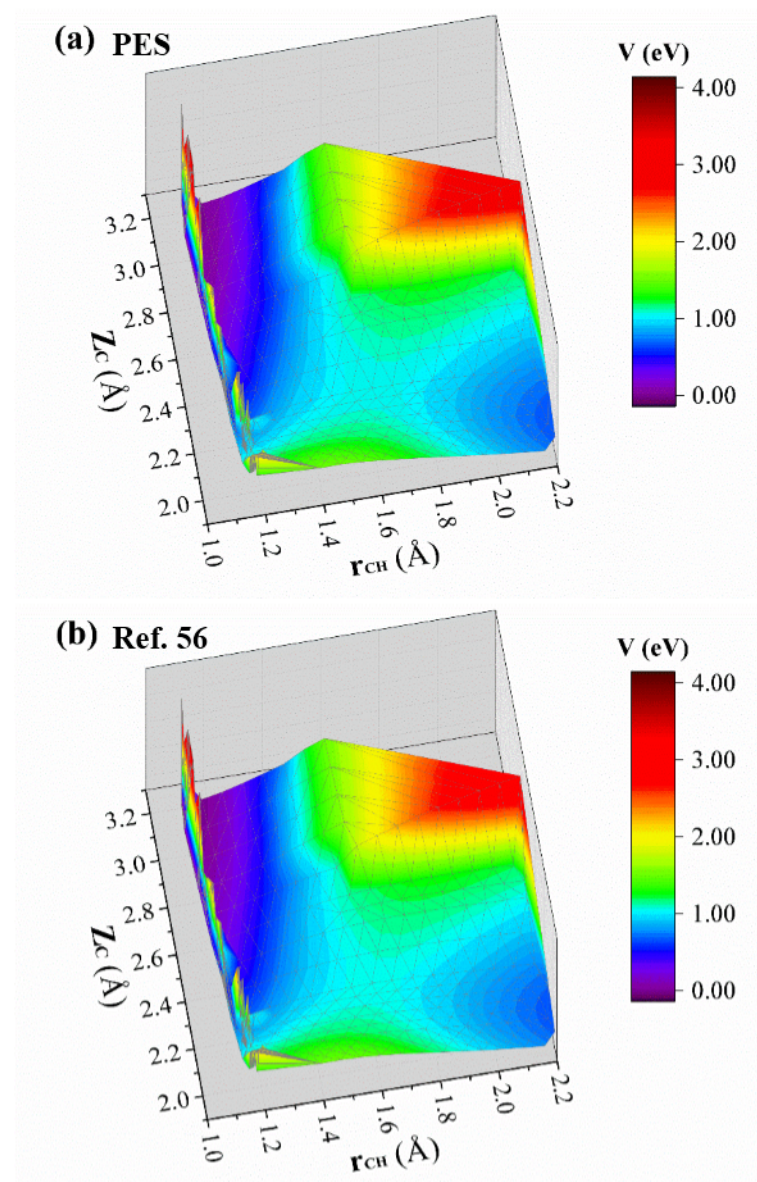


Fig. 5

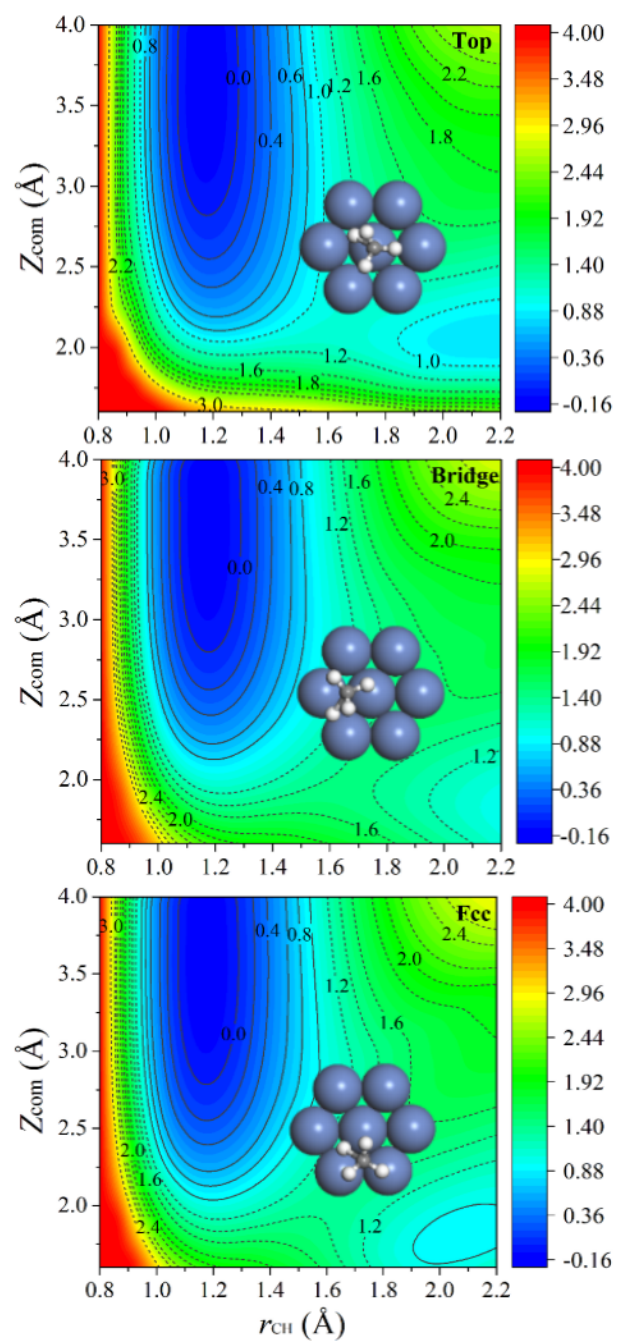


Fig. 6

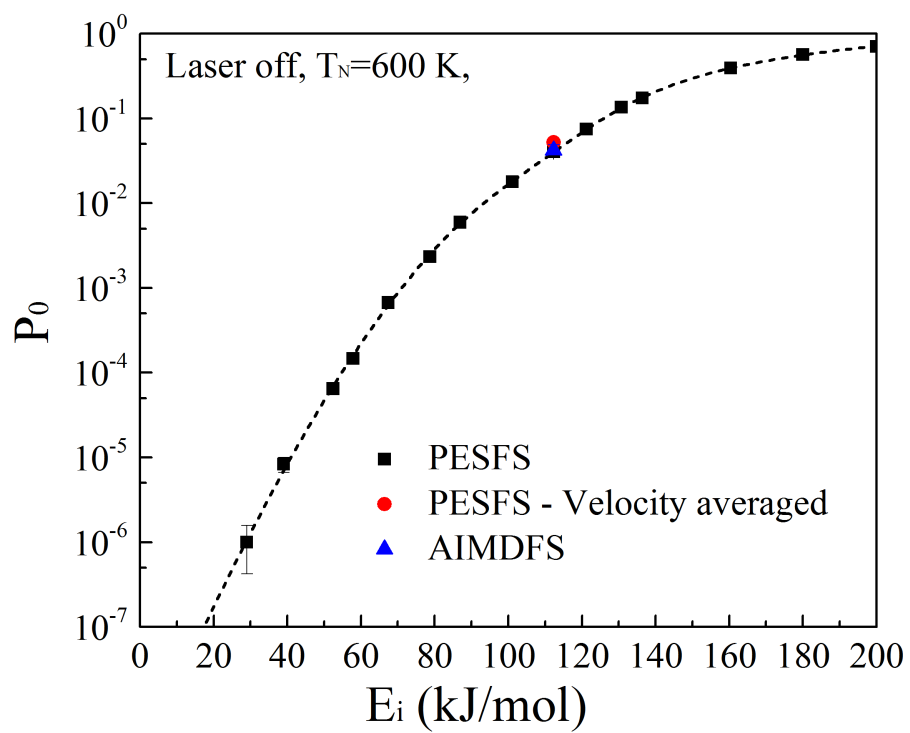


Fig. 7

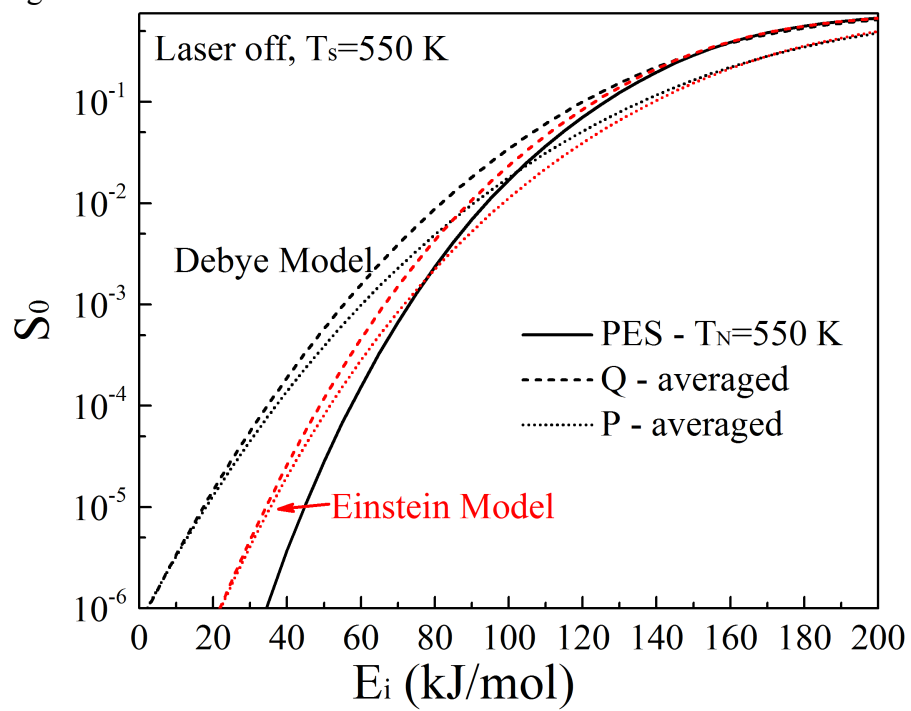
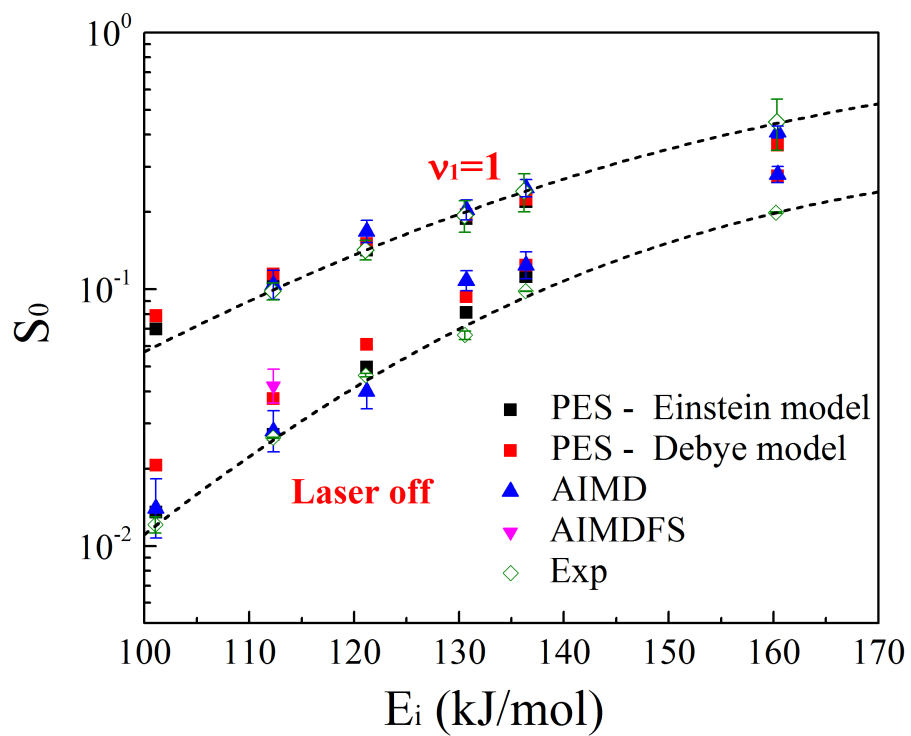
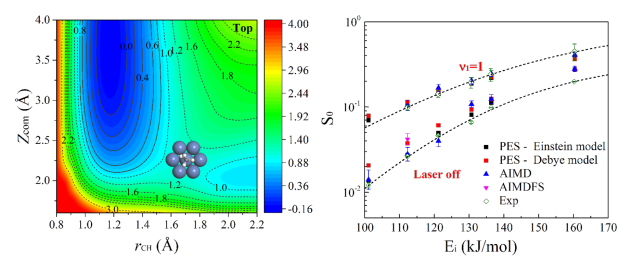


Fig. 8



TOC graphic



A new chemically accurate potential energy surface for the dissociative chemisorption of methane on the rigid Ni(111) surface.